



University of Nebraska - Lincoln

From the Selected Works of Serge Youri Kalmykov

Summer August 18, 2020

Radiation emission at Langmuir frequency from laser wake in longitudinally stratified plasma column

Serge Y Kalmykov

Jennifer Elle, *Air Force Research Laboratory*

Andreas Schmitt-Sody, *Air Force Research Laboratory*



Available at: https://works.bepress.com/serguei_kalmykov/65/

PAPER

Radiation emission at Langmuir frequency from laser wake in longitudinally stratified plasma column

To cite this article: Serge Kalmykov *et al* 2020 *Plasma Phys. Control. Fusion* **62** 115022

View the [article online](#) for updates and enhancements.



IOP | ebooks™

Bringing together innovative digital publishing with leading authors from the global scientific community.

Start exploring the collection—download the first chapter of every title for free.

Radiation emission at Langmuir frequency from laser wake in longitudinally stratified plasma column

Serge Kalmykov¹ , Jennifer Elle² and Andreas Schmitt-Sody²

¹ Leidos Innovations Center, Leidos Inc., Albuquerque, NM 87106, United States of America

² High Power Electromagnetics Division, Air Force Research Laboratory, Kirtland Air Force Base, NM 87117, United States of America

E-mail: serge.kalmykov@leidos.com

Received 23 June 2020, revised 5 August 2020

Accepted for publication 17 August 2020

Published 8 October 2020



CrossMark

Abstract

Theoretical analysis shows that a small-amplitude laser wake (an electrostatic Langmuir wave), driven in a periodically stratified, cylindrical plasma column, generates a superluminal, azimuthally polarized rotational current at a Langmuir frequency. The current radiates a radially polarized (i.e. transverse magnetic) Cherenkov signal into the plasma-free space. The opening angle of the Cherenkov emission cone is defined by the spatial period of stratification. Lifetime of the laser wake, limited by wave breaking in the inhomogeneous plasma, defines the terahertz (THz) signal length. This length ranges from a few picoseconds to hundreds of picoseconds, depending on the wake amplitude, amplitude of background density modulation, and stratification period. Monochromaticity and coherence distinguishes this THz signal from the ultrashort, uncollimated, broadband signals generated by photoionization currents in plasma filaments. The efficiency of electromagnetic energy conversion, from optical to THz, reaches its peak when the drive pulse waist size is close to the column radius. The efficiency increases with an increase in the drive pulse wavelength, and reaches the maximum when the drive pulse becomes near-critical for relativistic self-focusing. Numerical examples with sub-Joule, near-infrared terawatt drive pulses demonstrate the highest conversion efficiency of the order 10^{-5} , with the total emitted energy of several μJ , a few-hundred MV m^{-1} electric field at the column surface, and an MV m^{-1} field 10 cm away from the source.

Keywords: laser wake field, wave mode conversion, terahertz pulse, Cherenkov radiation, Smith-Purcell radiation

(Some figures may appear in colour only in the online journal)

1. Introduction

An electron flow, ponderomotively driven in a periodically stratified laser plasma (the plasma with an imprinted density grating), emits terahertz (THz) electromagnetic radiation, the emission pattern depending on the stratification period, radial inhomogeneity of the plasma, and the parameters of the drive laser pulse [1, 2]. Using plasma cur-

rents lifts limitations imposed by electrical breakdown, helping increase the THz signal power beyond the limits of solid structure-based sources [3, 4]. Since the inception of the field, generation of low-frequency radiation in the plasma had been associated with ponderomotively driven currents in the proximity of the drive laser pulse [1, 2, 4–6], resulting in broadband, uncollimated, yet short-pulse (femtosecond-scale) emission. Emission of multi-picosecond (ps), monochromatic,

megawatt (MW) THz beams, with an MV m^{-1} electric field in the wave zone, had been addressed sporadically, providing useful hints at the design of a theoretical framework [7, 8]. Notably, THz beams with these metrics have been produced in large-scale facilities, such as low-gain free-electron lasers (FELs) [9–12]. Their narrow bandwidth and tunability in frequency up to a few tens of THz are particularly attractive for driving long-lived material resonances [3, 13–15]. Application of long-pulse, high-field THz beams may be instrumental to increase and control, through impact ionization, free-carrier population in air [16, 17] and semiconductors [18, 19]. A GV m^{-1} electric field of a THz pulse within a mm-size dielectric structure can steer, pre-bunch, and accelerate an injected keV electron beam [20–22]. These manipulations of free electrons have been experimentally tested using single-cycle pulses at 0.3 THz central frequency. We conjecture that keeping a few-ps duration of the pulse while increasing the frequency by a factor of 10 to 30 (proportionally increasing the number of cycles) may result in electron beam slicing, generating trains of quasi-monoenergetic keV bunches [23].

The THz FELs are scarce and busy user facilities. Understanding the need in a compact source with similar metrics, we have theoretically explored a laser wake-mediated THz antenna. A near-infrared, femtosecond (fs) laser pulse (the ‘drive pulse’), propagating in a low-density plasma (10^{17} to 10^{19} electrons per cm^3), imparts a fraction of its energy (evaluated in Appendix A) into a long-lived, ponderomotively driven three-dimensional (3D) Langmuir wave—laser wake [24–26]. We show that the wake, driven in a periodically stratified plasma cylinder, emits into the free space a transverse magnetic (TM) Cherenkov signal at the Langmuir frequency (ranging from 2.8 to 28 THz for the above density range.) The opening angle of the Cherenkov cone is controlled by the stratification period. Matching the drive pulse waist size to the column radius maximizes the power of the signal and the efficiency of energy conversion from optical to THz.

The key element of the source—a cm-length plasma column with an imprinted density grating—may be produced by photoionization of stratified neutral gas by the same drive pulse [26, 27]. Stratification of the gas may be achieved by launching a MHz ultrasound wave [1, 28, 29], or by obstructing the gas flow from a slit nozzle [30] with an array of wires [31]. Alternatively, the stratified plasma column may be preformed using laser micro-machining, either by passing an ultrashort, high-intensity machining laser pulse (different from the drive pulse) through a patterned mask and imaging the mask onto the target plane [32], or by focusing an amplitude-modulated heater pulse through an axicon into a gas jet [2, 31]. In either case, an axially modulated breakdown, followed by shock waves expanding from the overheated, fully ionized regions, writes in the axial density modulation with a required period and amplitude.

Concentrating on the physics of THz emission, we remind that, so long as the background density of the plasma is uniform, the low-amplitude laser wake is purely electrostatic; it neither absorbs nor emits electromagnetic waves [33–35]. The wake current oscillates at a Langmuir frequency,

$\omega_{\text{pe}0} = (4\pi en_{e0}/m_e)^{1/2}$. Its phase velocity equals the group velocity of the drive pulse, $v_{g0} = \varepsilon_L^{1/2} c < c$. Here, n_{e0} is the background electron density; e and m_e are the electron charge and rest mass; $\varepsilon_L = 1 - \omega_{\text{pe}0}^2/\omega_0^2$ is the linear dielectric permittivity of the plasma; $\omega_0 \gg \omega_{\text{pe}0}$ is the fundamental frequency of the drive laser pulse; and c is the speed of light in vacuum. The fundamental wave number of the current is thus $k_p^{(0)} = \varepsilon_L^{-1/2} k_{p0}$, with $k_{p0} = \omega_{\text{pe}0}/c$. Inhomogeneity of the background makes laser wake fields partly electromagnetic, owing to the coupling of low-frequency electron velocity oscillations to the gradient in the background electron density [35–38]. If the background is axially uniform, the group velocity of the pulse and the phase velocity of the wake are subluminal. Hence, the TM signal accompanying the wake is radially evanescent [35]. A small-amplitude longitudinal modulation of the background, having a spatial period $2\pi K^{-1}$ (such as $K < k_{p0}$), alters the character of the signal. To the first order in the density modulation amplitude, the rotational current of the wake oscillates at the same fundamental Langmuir frequency $\omega_{\text{pe}0}$. Yet, the preset density grating splits this current into components with the up- and down-shifted wave numbers, $k_{z\pm} = k_p^{(0)} \pm K$. The component with a superluminal phase velocity, $v_{\text{ph}}^{(-)} = \omega_{\text{pe}0}/k_{z-} > c$, emits a cylindrical TM wave into the plasma-free space, the emission cone opening at a Cherenkov angle, $\theta_{\text{Ch}} = \arccos(c/v_{\text{ph}}^{(-)})$ [39]. The TM wave is monochromatic, obeying the free-space dispersion equation, $\omega_{\text{pe}0} = ck_{p0}$. The emitted radiation is thus akin to Smith-Purcell radiation, occurring when a spatial modulation of the medium imparts a superluminal component to the externally driven oscillatory rotational current, causing Cherenkov emission at the current oscillation frequency [40].

This paper develops an accurate perturbative description of Cherenkov emission in the experimentally relevant, cylindrical 3D geometry. The key finding is that the efficiency of energy conversion from optical to THz is highly sensitive to the ratio of the drive pulse waist size r_0 to the column radius R_{col} , dubbed the aspect ratio, $\mathcal{R} = r_0/R_{\text{col}}$. In contrast to the statements based on the two-dimensional (2D) Cartesian model [8], the most efficient conversion occurs at $\mathcal{R} \approx 1$. (This promises easier implementation, as plasma columns with such aspect ratio are created naturally, by the drive pulse itself, through photoionization of the ambient neutral gas [25, 35, 38]). For similar interaction regimes, the energy conversion is at least an order of magnitude less efficient in the cylindrical system than in the 2D planar one. Yet, our predictions of $\sim 10^{-5}$ efficiency, up to a few μJ in a few-ps THz signal, and an MV m^{-1} -scale electric field ten centimeters away from the source are competitive with other plasma-based sources [4], with a favorable distinction of monochromaticity and coherence. These top metrics are expected when operating near a threshold for relativistic self-focusing of the drive pulse [41], using a sufficiently short-wavelength density grating ($K \approx k_{p0}$, $\theta_{\text{Ch}} \approx 90^\circ$).

The presentation is structured as follows. Section 2 describes the physical system—a longitudinally stratified plasma column and a cylindrical, electromagnetic plasma

wake driven by the ponderomotive force of a short laser pulse. The electric and magnetic fields of the wake are linear in the drive pulse intensity. Stratification has the form of a pre-set, radially inhomogeneous sinusoidal grating. The density variation in the grating is assumed to be small; the wake fields are calculated to the first order in the small stratification amplitude. The zero-order terms are conventional electrostatic wake fields in the piecewise uniform plasma [24]; they contribute to the rotational current—the source of first-order rotational fields. Sub- and superluminal components of the source are identified, and Bessel-type equations are derived for the amplitudes of the source-driven magnetic fields. Section 3 proves that the plasma must be radially bounded ($R_{\text{col}} < \infty$) to permit Cherenkov emission at the Langmuir frequency. The latter is the subject of section 4. Section 4.1 presents analytical solutions for the field amplitudes and their far-field asymptotic. It is pointed out that the aspect ratio $\mathcal{R} \approx 1$ maximizes the field amplitude in the plasma-free space. It is also shown that a weak transverse inhomogeneity of stratification increases the Cherenkov signal. Section 4.2 evaluates the power of the THz pulse and the rate of wake depletion due to Cherenkov emission. The depletion rate, dependent on geometric aspects only (i.e. the laser pulse waist size and the column radius), is found to be rather weak, with merely a few percents of wake energy converted into the electromagnetic signal. Section 4.3 evaluates the efficiency of energy conversion from optical to THz, assuming that the wake lifetime (the THz signal length) is limited by the Langmuir wave breaking in the inhomogeneous plasma [42, 43]. Similarly to the wake depletion time, the conversion efficiency is entirely defined by the geometry of the system. The power and energy of the THz signal steadily grow as the Cherenkov angle increases and the aspect ratio \mathcal{R} tends to unity. Dependence of the efficiency on the laser wavelength and mean background density reveals some advantage in driving the wake with mid-infrared ultrashort laser pulses [44, 45]. Section 5 examines the trends in THz signal metrics for the drive pulse of fixed intensity. In this setting, by varying the pulse waist size one varies the pulse power. Again, it is shown that optimizing the energy conversion (reaching the efficiency of order 10^{-5}) needs matching the column and drive pulse waist sizes, $\mathcal{R} \approx 1$. Finally, operating near the relativistic self-focusing threshold maximizes the signal power (a few MW) and radiated energy (several μJ). Section 6 sums up the results and points out the directions of future work.

2. Theoretical model

2.1. Definitions and introductory remarks

We explore events in a transversely bounded plasma without an external magnetic field or direct current (their effect is considered elsewhere [46].) One example is a flat-top column created by photoionization of the ambient gas by the drive laser pulse [25, 26]. We focus on electron currents behind the driver; the background plasma is thus assumed stationary.

This neglects dissipation of the column on a nanosecond scale, as the pressure gradient [47], charged particle diffusion into the neutral gas [48], or the ponderomotive force of the laser wake [49] set ions in motion; these slow dynamics may be treated perturbatively elsewhere. The plasma is characterized by distributions of electron number density $n_e(t, \mathbf{r})$, electron fluid velocity $\mathbf{v}(t, \mathbf{r})$ (non-relativistic, $|\mathbf{v}| \ll c$), and current density $\mathbf{j} = en_e\mathbf{v}$, where $\mathbf{r} = (x, y, z)$. The background electron density $n_{\text{bg}}(\mathbf{r})$ defines a spatially non-uniform Langmuir frequency $\omega_{\text{pe}}(\mathbf{r}) = n^{1/2}\omega_{\text{pe}0}$ and a wave number $k_p(\mathbf{r}) = \omega_{\text{pe}}/c = n^{1/2}k_{p0}$, where $n(\mathbf{r}) = n_{\text{bg}}/n_{e0}$. The constant reference density n_{e0} (such as the average electron density on the pulse propagation axis) defines the reference plasma frequency $\omega_{\text{pe}0}$ and the wave number k_{p0} . The plasma electrons receive a push from the drive pulse ponderomotive force. The resulting violation of quasi-neutrality sets up electron currents (laser wake) that vary on a sub-picosecond scale, while the ions remain at rest, forming an inhomogeneous neutralizing background.

The laser wake fields may contain both potential (electrostatic) and rotational (electromagnetic) components. In the low-density plasma, they vary slowly over the optical period, $2\pi\omega_0^{-1}$. The rotational wake field, second-order in the drive pulse amplitude (linear in intensity) emerges from coupling the electron velocity oscillations in the wake to the gradient of the background density, ∇n_{bg} [1, 35]. In the plasma with a radially stratified yet axially uniform stationary background, the electromagnetic component of the wake is a radially evanescent TM mode, detectable a few millimeters away from axis [35, 46]. The evanescence is due to the fact that the low-frequency rotational current in the plasma has a subluminal phase velocity equal to phase velocity of the wake, which, in turn, equals the slightly sub-luminal group velocity of the drive laser pulse. To turn the rotational wake field into an obliquely propagating TM wave, one has to ‘accelerate’ the rotational current, making its phase velocity superluminal. This may be accomplished by imprinting a density grating into the background plasma as described in the Introduction.

At this point, it is convenient to introduce normalized variables. Through the remainder of the paper, all lengths and parameters with the dimension of length are normalized to k_{p0}^{-1} ; time and all parameters with the dimension of time to $\omega_{\text{pe}0}^{-1}$; all velocities to the speed of light in vacuum c ; and the low-frequency fields to $E_{\text{br}} = m_e\omega_{\text{pe}0}c/|e| = 96(n_{e0}[\text{cm}^{-3}])^{1/2} \text{ V m}^{-1}$, the field corresponding to wave breaking of a non-relativistic, one-dimensional (1D) Langmuir wave in the cold plasma [50]. Plasma density is normalized to n_{e0} . The normalized parameters and dependent variables (such as field amplitudes and electron velocities) shall wear hats. So long as confusion is unlikely, the notations for the independent variables (e.g. x, y, z) will be the same, the normalization to be clear from the context. With these conventions in mind, background electron density of the cylindrically symmetric, stratified plasma with a sharp edge is defined

as $n(r_\perp, z) = \hat{n}(r_\perp, z)H(\hat{R}_{\text{col}} - r_\perp)$, where H is the Heaviside step-function, and

$$\hat{n} = 1 + \alpha F(r_\perp) \sin(\hat{K}z). \quad (1)$$

Here, $r_\perp^2 = x^2 + y^2$, $\alpha \ll 1$ is the density modulation amplitude, and $\hat{K} < 1$ is the stratification wave number. A radial inhomogeneity of stratification, not uncommon in experimental settings [31], is mimicked with a factor $F = e^{-2\beta\hat{K}(r_\perp/\hat{r}_0)^2}$, where a constant β not necessarily small, and \hat{r}_0 is the waist size of the Gaussian drive laser pulse,

$$a(\zeta, r_\perp) = a_0 e^{-(r_\perp/\hat{r}_0)^2} e^{-\zeta^2/(2L)^2}. \quad (2)$$

The pulse propagates toward positive z at a group velocity v_{g0} , hence the propagation variable $\zeta = z - v_{g0}t$ (in the dimensional form, $\zeta = z - v_{g0}t$). Envelope (2) of the pulse electric field (normalized to $m_e\omega_0 c/|e|$) is accurate in the vicinity of the focal plane, $|z| \ll \hat{Z}_R$, where $\hat{Z}_R = (\hat{r}_0^2/2)(1 - \varepsilon_L)^{-1/2}$ is the normalized Rayleigh length. Operating near a threshold for relativistic self-focusing [41],

$$a_0 \leq a_{\text{cr}} = 2^{5/2}\hat{r}_0^{-1}, \quad (3)$$

helps roughly preserve the shape of the pulse (2) in a cm-length open system [30].

We remark, finally, that the assumed discontinuity in the plasma density at the column edge is an idealization. In reality, the density of plasma species falls off within a thin shell, $|r_\perp - \hat{R}_{\text{col}}| = \hat{\Delta}_{\text{sh}}$, with $\hat{\Delta}_{\text{sh}} \ll 1$. The electron flow, as well as the potential electric field and its derivatives, remain continuous within the shell [35, 38, 46]; this avoids such artifacts as the ‘surface wakefield’ [51] or ‘electromagnetic pulse in the steady state regime’ [7]. Meanwhile, stratification of the bulk plasma (1) generates a low-frequency azimuthal magnetic field both within and without the column. Continuity of electron flow keeps radial derivative of this field continuous at the interface $r_\perp = \hat{R}_{\text{col}}$.

One may note that the steep density gradient within the shell supports a rotational current of its own [35, 46]. This current, having no singularities, vanishes in the limit $\hat{\Delta}_{\text{sh}} \rightarrow 0$. Hence, so long as $\hat{\Delta}_{\text{sh}} \ll 1$, the currents in the boundary layer contribute little to the low-frequency TM signal. (Apart from that, any radiation coming from these currents would belong to the low-frequency band, $0 < \hat{\omega} < 1$ [35, 46], will have large angular spread, and will be thus clearly distinguishable from a monochromatic, with $\hat{\omega} = 1$, emission strictly at the Cherenkov angle.)

2.2. Low-frequency electromagnetic wake fields

The task is to describe the slowly varying electromagnetic field, driven by the currents induced in the plasma by the ponderomotive force of a short, intense optical pulse (2). The procedure [35] may be summarized as follows. The electron current, second-order in the laser pulse amplitude, slowly varying over the optical cycle, $\langle \mathbf{j} \rangle \sim \mathcal{O}(a^2)$ (angular brackets meaning time averaging), is proportional to a sum of ponderomotively and magnetically-driven electron velocities, $\hat{\mathbf{v}}_p$ and $\hat{\mathbf{v}}_B$. Hydrodynamics of a cold electron fluid, describing the linear response to the laser ponderomotive force and to the slowly varying electric and magnetic fields, yield the following equations for the velocities,

$$(\partial^2/\partial t^2 + n)\hat{\mathbf{v}}_p = -(1/4)\nabla\partial a^2/\partial t, \quad (4)$$

$$\nabla \times \hat{\mathbf{v}}_B = -\hat{\mathbf{B}},$$

where $\hat{\mathbf{B}}$ is the (normalized) low-frequency magnetic field, the object of our study. Remembering that this magnetic field is driven by the curl of a slowly varying rotational current [52], $(\partial^2/\partial t^2 - \nabla^2)\hat{\mathbf{B}} = \nabla \times (n\hat{\mathbf{v}})$, we arrive at the centerpiece of our model [35],

$$(\nabla^2 - \partial^2/\partial t^2 - \hat{n})\hat{\mathbf{B}} + (\nabla\hat{n}) \times \hat{\mathbf{v}}_B = -(\nabla\hat{n}) \times \hat{\mathbf{v}}_p \equiv \mathbf{S}, \quad (5)$$

$$(\nabla^2 - \partial^2/\partial t^2)\hat{\mathbf{B}} = 0. \quad (6)$$

Equations (5) and (6) define the field within ($r_\perp \leq \hat{R}_{\text{col}}$) and without the column ($r_\perp > \hat{R}_{\text{col}}$), respectively. Magnetic field and its derivatives are continuous at the interface.

A cylindrically symmetric ponderomotive force of the driver (2) does not impart an azimuthal component to the electron velocity (4). With $\hat{\mathbf{v}}_p(t, r_\perp, z) = \mathbf{e}_r\hat{v}_{pr} + \mathbf{e}_z\hat{v}_{pz}$, the source of the magnetic field is azimuthally polarized:

$$\mathbf{S} = -\mathbf{e}_\phi[\hat{v}_{pr}(\partial\hat{n}/\partial z) - \hat{v}_{pz}(\partial\hat{n}/\partial r_\perp)] \equiv \mathbf{e}_\phi S_\phi,$$

$$S_\phi = -\alpha\hat{K}e^{-2\beta\hat{K}(r_\perp/\hat{r}_0)^2} \left[\hat{v}_{pr} \cos(\hat{K}z) + 4\beta(r_\perp/\hat{r}_0^2)\hat{v}_{pz} \sin(\hat{K}z) \right]. \quad (7)$$

Here, $\mathbf{e}_r = \mathbf{e}_x \cos \phi + \mathbf{e}_y \sin \phi$ is the radial unit vector of a cylindrical framework, and ϕ is the azimuthal angle, with the corresponding unit vector $\mathbf{e}_\phi = -\mathbf{e}_x \sin \phi + \mathbf{e}_y \cos \phi$. The magnetic field is thus purely azimuthal, while the electric field has radial and longitudinal components coming from the Ampère’s Law [35]. The electromagnetic mode we are looking for is thus a cylindrical TM mode, with the magnetic field obeying equations

$$\begin{aligned} & [\nabla_\phi^2 - (\partial^2/\partial t^2 + \hat{n})] \hat{B}_\phi + \hat{v}_{Br}(\partial\hat{n}/\partial z) \\ & - \hat{v}_{Bz}(\partial\hat{n}/\partial r_\perp) = S_\phi, \end{aligned} \quad (8)$$

$$(\nabla_\phi^2 - \partial^2/\partial t^2) \hat{B}_\phi = 0. \quad (9)$$

Here, $\nabla_\phi^2 = \partial^2/\partial z^2 + \partial^2/\partial r_\perp^2 + r_\perp^{-1}\partial/\partial r_\perp - r_\perp^{-2}$ is the azimuthal component of the vector Laplacian. Quasistatic solutions [35] of equation (4) yield the components of electron velocity behind the drive pulse:

$$\begin{aligned} \hat{v}_{pr}(\zeta < -\hat{L}) & \approx -G(\hat{n}, \hat{L})(4r_\perp/\hat{r}_0^2) e^{-2(r_\perp/\hat{r}_0)^2} \\ & \cos\left[\hat{n}^{1/2}(\varepsilon_L^{-1/2}z - t)\right], \end{aligned} \quad (10)$$

$$\begin{aligned} \hat{v}_{pz}(\zeta < -\hat{L}) & \approx -G(\hat{n}, \hat{L})(\hat{n}/\varepsilon_L)^{1/2} e^{-2(r_\perp/\hat{r}_0)^2} \\ & \sin\left[\hat{n}^{1/2}(\varepsilon_L^{-1/2}z - t)\right]. \end{aligned} \quad (11)$$

Here, $G(\hat{n}, \hat{L}) = a_0^2[\pi/(8\varepsilon_L)]^{1/2} \hat{L} e^{-\hat{n}\hat{L}^2/(2\varepsilon_L)}$. So long as $\hat{r}_0 > 2e^{-1/2}$, the wake is quasi-longitudinal, meaning $|\hat{v}_{pr}| < |\hat{v}_{pz}|$. Periodic stratification (1) imparts periodic phase modulation into velocities (10) and (11), generating spectral satellites shifted by integer multiples of the modulation wave number, $\hat{k}_{zm} = \varepsilon_L^{-1/2} \pm m\hat{K}$. As the amplitude of m th satellite is of the order α^m , $m = 1, 2, \dots$ [53, 54], its contribution to the rotational current (the source (7)) is of the order α^{1+m} . Therefore, evaluating the source to the leading (first) order in α , one needs only the fundamental harmonic of the wake. The latter is obtained by setting $\hat{n} \equiv 1$ in equations (10) and (11).

Treating the effect of stratification perturbatively, we express the source, the fields, and the velocities as a power series $f = \sum_0^\infty (\alpha\hat{K})^m f^{(m)}$, $m=0$ corresponding to solutions in the piecewise uniform plasma. To the lowest order, $S_\phi \approx \alpha\hat{K}G_0(S_{\phi+} + S_{\phi-})$ with

$$\begin{aligned} S_{\phi\pm} & = (1 \mp \varepsilon_L^{-1/2}\beta)(2r_\perp/\hat{r}_0^2) e^{-2(1+\beta\hat{K})(r_\perp/\hat{r}_0)^2} \\ & \cos(\hat{k}_{z\pm}z - t), \end{aligned} \quad (12)$$

$$\hat{k}_{z\pm} = \varepsilon_L^{-1/2} \pm \hat{K},$$

where $G_0 = G(1, \hat{L})$. For the stratification wave number slightly above zero, $\hat{K} > \varepsilon_L^{-1/2} - 1$, the ‘negative’ branch of the source has a superluminal phase velocity, $\hat{v}_{ph}^{(-)} = \hat{k}_{z-}^{-1} > 1$. Magnetic field driven by this branch corresponds to Cherenkov emission, the focus of our study. The other branch is subluminal, having a phase velocity $\hat{v}_{ph}^{(+)} = \hat{k}_{z+}^{-1} < 1$; it drives the radially evanescent TM mode, akin to the one described earlier [35, 46].

In the piecewise uniform plasma, the magnetic field and rotational velocity of electron fluid are identically zero,

$\hat{B}_\phi^{(0)} = \hat{v}_{Br}^{(0)} = \hat{v}_{Bz}^{(0)} \equiv 0$ [35]. The phase of the source (12) dictating the phase of the forced solution, the first-order magnetic field reads

$$\hat{B}_\phi \approx \alpha\hat{K}G_0 \text{Re} \left(\mathcal{B}^{(+)}(r_\perp) e^{i(\hat{k}_{z+}z - t)} + \mathcal{B}^{(-)}(r_\perp) e^{i(\hat{k}_{z-}z - t)} \right). \quad (13)$$

From equation (8), the magnetic field amplitudes in the plasma, $\mathcal{B}_{in}^{(\pm)} = \mathcal{B}^{(\pm)}(r_\perp \leq \hat{R}_{col})$, obey the nonhomogeneous modified Bessel equations

$$(\hat{\mathcal{L}} - \hat{k}_{z\pm}^2) \mathcal{B}_{in}^{(\pm)} = (1 \mp \varepsilon_L^{-1/2}\beta)(2r_\perp/\hat{r}_0^2) e^{-2(1+\beta\hat{K})(r_\perp/\hat{r}_0)^2},$$

where $\hat{\mathcal{L}} = d^2/dr_\perp^2 + r_\perp^{-1}d/dr_\perp - r_\perp^{-2}$. The regular at the origin solution reads

$$\mathcal{B}_{in}^{(\pm)} = C_I^\pm I_1(\hat{k}_{z\pm}r_\perp) + \mathcal{B}_{forced}^{(\pm)}(\hat{R}_{col}, r_\perp), \quad (14)$$

$$\mathcal{B}_{forced}^{(\pm)} = - (1 \mp \varepsilon_L^{-1/2}\beta) \left[K_1(\hat{k}_{z\pm}r_\perp) \mathcal{I}_I^\pm + I_1(\hat{k}_{z\pm}r_\perp) \mathcal{I}_K^\pm \right]. \quad (15)$$

In equation (14), C_I^\pm is a constant, and I_1 and K_1 are the modified Bessel functions of the first and second kind, respectively [55]. A Green’s function for the modified Bessel equation [56, 57] defines the integrals

$$\mathcal{I}_I^\pm(r_\perp) = 2 \int_0^{r_\perp} I_1(\hat{k}_{z\pm}s)(s/\hat{r}_0)^2 e^{-2(1+\beta\hat{K})(s/\hat{r}_0)^2} ds, \quad (16)$$

$$\mathcal{I}_K^\pm(\hat{R}_{col}, r_\perp) = 2 \int_{r_\perp}^{\hat{R}_{col}} K_1(\hat{k}_{z\pm}s)(s/\hat{r}_0)^2 e^{-2(1+\beta\hat{K})(s/\hat{r}_0)^2} ds. \quad (17)$$

The free-space field $\mathcal{B}_{out}^{(+)} = \mathcal{B}^{(+)}(r_\perp > \hat{R}_{col})$, coupled to the sub-luminal mode $\mathcal{B}_{in}^{(+)}$, is exponentially evanescent and thus physically unremarkable. This field is the solution to the homogeneous modified Bessel equation $(\hat{\mathcal{L}} - \hat{k}_{z+}^2)\mathcal{B}_{out}^{(+)} = 0$ with $\hat{k}_{z+}^2 = \hat{k}_{z+}^2 - 1 > 0$, the corollary of equation (9). The regular at infinity solution, $\mathcal{B}_{out}^{(+)} \sim K_1(\hat{k}_{z+}r_\perp) \sim [\pi/(2\hat{k}_{z+}r_\perp)]^{1/2} e^{-\hat{k}_{z+}r_\perp}$, decays at a rate $\hat{k}_{z+} \sim \hat{K}^{1/2}$. As a result, the mode $\mathcal{B}_{out}^{(+)}$ extends into the free space no further than a few plasma wavelengths.

Conversely, the superluminal source drives the magnetic field that is not evanescent in the free space. Per equation (9), its amplitude obeys the Bessel equation,

$$(\hat{\mathcal{L}} + \hat{k}_r^2) \mathcal{B}_{out}^{(-)} = 0, \quad (18)$$

with the positive constant

$$\hat{k}_r^2 = 1 - \hat{k}_{z-}^2 = \hat{K}(2 - \hat{K}). \quad (19)$$

The general solution of equation (18) is a linear combination of Bessel functions of the first (J_1) and second kind (Y_1). One particular combination, the Hankel function $H_1^{(1)}(\hat{k}_r r_\perp) = J_1(\hat{k}_r r_\perp) + iY_1(\hat{k}_r r_\perp)$, has an asymptotic corresponding to the outgoing wave, $H_1^{(1)}(\hat{k}_r r_\perp \rightarrow \infty) \approx e^{-3\pi i/4} [2/(\pi \hat{k}_r r_\perp)]^{1/2} e^{i\hat{k}_r r_\perp}$ (cf the asymptotic (8.451.3) of [55].) This cylindrical TM wave has a frequency equal to the mean Langmuir frequency, $\hat{\omega} = 1$, and propagates at a Cherenkov angle [39],

$$\theta_{\text{Ch}} = \arccos(\hat{k}_{z-}/|\hat{\mathbf{k}}|) = \arccos(1/\hat{v}_{\text{ph}}^{(-)}), \quad (20)$$

where $|\hat{\mathbf{k}}|^2 = \hat{k}_{z-}^2 + \hat{k}_r^2 = 1$. Cherenkov emission—the focus of our paper—is sketched in figure 1; its properties and physical implications are the subject of section 4.

To afford periodic stratification, the plasma must be longer than the grating period: $\hat{K} > \hat{K}_{\text{min}} = 2\pi\hat{L}_{\text{pl}}^{-1}$. With the diffraction-limited $\hat{L}_{\text{pl}} \approx \hat{Z}_R \gg 1$, the emission angles exceed

$$\theta_{\text{Ch}}^{\text{min}} \approx (2\hat{K}_{\text{min}})^{1/2} \approx (8\pi)^{1/2} (1 - \varepsilon_L)^{1/4} \hat{r}_0^{-1}. \quad (21)$$

Finally, calculating the energy flux density needs the electric field of the outgoing wave,

$$\hat{\mathbf{E}}^{(\text{rad})} = \alpha \hat{K} G_0 \text{Re} \left[(\mathbf{e}_r \mathcal{E}_r^{(-)} + \mathbf{e}_z \mathcal{E}_z^{(-)}) e^{i(\hat{k}_z z - t)} \right]. \quad (22)$$

The Ampère's Law yields $\mathcal{E}_r^{(-)} = \hat{k}_{z-} \mathcal{B}_{\text{out}}^{(-)}$, and $\mathcal{E}_z^{(-)} = i r_\perp^{-1} d(r_\perp \mathcal{B}_{\text{out}}^{(-)})/dr_\perp$.

3. Transversely unbounded plasma: wake-driven TM signal is evanescent

In the transversely unbounded plasma, the regular in the entire space magnetic field is given by the forced solution (15), with $\hat{R}_{\text{col}} = \infty$ in the integral (17). The analysis of this solution in Appendix B yields the radially evanescent asymptotic,

$$\mathcal{B}_{\text{forced}}^{(\pm)}(\hat{R}_{\text{col}} = \infty, r_\perp \rightarrow \infty) \approx -\mathcal{B}_0^{(\pm)} [\pi/(2\hat{k}_{z\pm} r_\perp)]^{1/2} e^{-\hat{k}_{z\pm} r_\perp}, \quad (23)$$

where $\mathcal{B}_0^{(\pm)} = (1 \mp \varepsilon_L^{-1/2} \beta) [\hat{k}_{z\pm} (1 + \beta \hat{K})]^{-1} u_\pm e^{u_\pm}$, and $u_\pm = (\hat{k}_{z\pm} \hat{r}_0)^2 [8(1 + \beta \hat{K})]^{-1}$. The asymptotic (23) holds for $r_\perp > 4\hat{k}_{z\pm}^{-1} u_\pm$. One can see that, regardless of its longitudinal phase velocity, the signal (23) does not propagate away from the source. Far away from axis, it obeys the dispersion equation of an electromagnetic wave, $\hat{\omega}^2 = 1 + \hat{k}_r^2 + \hat{k}_{z\pm}^2$. As the frequency of the signal is strictly the average Langmuir frequency ($\hat{\omega}^2 = 1$, per equation (13)), the radial wave number is imaginary, $\hat{k}_r = i\hat{k}_{z\pm}$; this defines the asymptotic decay rate of the solution (23). Hence, to permit radiation emission at the plasma frequency, the plasma has to be radially bounded, $\hat{R}_{\text{col}} < \infty$.

This conclusion accords with the earlier finding [1] that a long-wavelength density grating ($\hat{K} < 1$), imprinted into the infinite and radially homogeneous plasma, produces only near-forward, broadband emission of waves with the frequencies well above the mean Langmuir frequency. These high-frequency waves, naturally, may not originate in the wake zone, $\zeta < -\hat{L}$, where the monochromatic radiation source (12) oscillates at the Langmuir frequency. The only other location is the neighborhood of the drive pulse, $-\hat{L} < \zeta < \hat{L}$, on which the paper [1] concentrates. At this location, the frequency spectrum of electron velocity perturbations is dictated by the spectrum of the pulse ponderomotive force. The latter contains a continuum of components above the mean Langmuir frequency. The high-frequency components of the ponderomotive current, in the presence of long-wavelength stratification, may become superluminal, making up a source of an obliquely propagating broadband signal [1].

4. Transversely bounded plasma: superluminal source emits Cherenkov signal

4.1. Electric and magnetic fields in plasma-free space

If the plasma is bounded, $\hat{R}_{\text{col}} < \infty$, the magnetic field $\mathcal{B}_{\text{in}}^{(-)}$, driven by the superluminal source within the column, is defined by the expression (14) with a nonzero C_I^- . Equation (18) and the Ampère's Law define the regular at infinity free-space fields:

$$\mathcal{B}_{\text{out}}^{(-)} = \hat{k}_{z-}^{-1} \mathcal{E}_r^{(-)} = C_H H_1^{(1)}(\hat{k}_r r_\perp), \quad (24)$$

$$\mathcal{E}_z^{(-)} = i\hat{k}_r C_H H_0^{(1)}(\hat{k}_r r_\perp). \quad (25)$$

Here, C_H is a complex constant; $H_m^{(1)}(\hat{k}_r r_\perp) = J_m(\hat{k}_r r_\perp) + iY_m(\hat{k}_r r_\perp)$, $m = 0, 1$, are the Bessel functions of the third kind (the Hankel functions); and J_m and Y_m are the Bessel functions of the first and second kind, respectively. Continuity of the magnetic field and its derivative at the column surface defines the constants,

$$C_I^- = \frac{w H_0^{(1)}(w) K_1(v) + v K_0(v) H_1^{(1)}(w)}{w H_0^{(1)}(w) I_1(v) - v I_0(v) H_1^{(1)}(w)} (1 + \varepsilon_L^{-1/2} \beta) \mathcal{I}_I^-(\hat{R}_{\text{col}}),$$

$$C_H = \frac{(1 + \varepsilon_L^{-1/2} \beta) \mathcal{I}_I^-(\hat{R}_{\text{col}})}{w H_0^{(1)}(w) I_1(v) - v I_0(v) H_1^{(1)}(w)}, \quad (26)$$

where $v = \hat{k}_{z-} \hat{R}_{\text{col}}$, and $w = \hat{k}_r \hat{R}_{\text{col}}$. Asymptotic expressions for C_H , corresponding to the near-forward and lateral emission, are derived in Appendices C and D. The amplitudes (24) and (25) yield the radiation vector fields in the wave zone, $\hat{k}_r r_\perp \gg 1$:

$$\hat{\mathbf{B}}^{(\text{rad})} \approx -\mathbf{e}_\phi \mathcal{Z}(t, r_\perp, z), \quad (27)$$

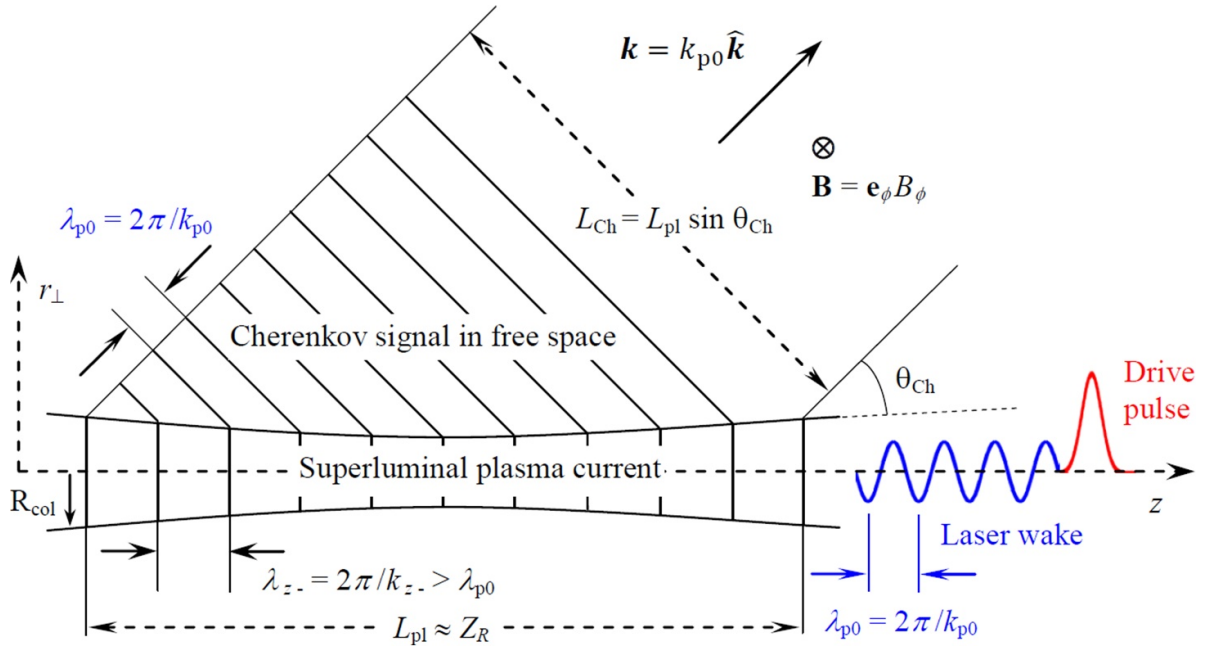


Figure 1. A sketch of Cherenkov emission (in the plane containing the laser pulse propagation axis; not in scale.) The superluminal rotational current, bound to the plasma column, emits a hollow beam of Cherenkov radiation (with the azimuthally polarized magnetic field); the Cherenkov radiation wavelength equals the wavelength of the laser wake λ_{p0} . The radiation fills a conical shell with a width L_{Ch} and an opening angle θ_{Ch} .

$$\hat{\mathbf{E}}^{(\text{rad})} \approx -(\mathbf{e}_r \hat{k}_{z-} - \mathbf{e}_z \hat{k}_r) \mathcal{Z}(t, r_{\perp}, z). \quad (28)$$

Here, $\mathcal{Z} = \alpha \hat{K} G_0 [2/(\pi \hat{k}_r r_{\perp})]^{1/2} \text{Re}(C_H e^{i(\hat{\mathbf{k}}\mathbf{r} - t + \pi/4)})$, and $\hat{\mathbf{k}} = \mathbf{e}_r \hat{k}_r + \mathbf{e}_z \hat{k}_{z-}$. The outgoing conical TM wave, described by equations (27) and (28), defines the emission pattern sketched in figure 1.

Numerical demonstrations through the remainder of the paper will be made for the radially homogeneous stratification, $\beta = 0$ (except for figure 3), with a density grating amplitude $\alpha = 0.1$ (this weak modulation is easily accessible with any of the methods listed in the Introduction.) As a driver, we select the laser pulse with a wavelength $\lambda_0 = 0.8 \mu\text{m}$, full width at half-maximum (FWHM) in intensity $\tau_L = (8 \ln 2)^{1/2} L/c = 31.5 \text{ fs}$, and a marginally sub-relativistic peak intensity $I_{\text{max}} \approx 1.06 \times 10^{18} \text{ W cm}^{-2}$ ($a_0 = 0.7$). We shall also keep unchanged the average density of the background plasma, $n_{e0} = 1.75 \times 10^{18} \text{ cm}^{-3}$ (so that $\varepsilon_L = 0.999$; the wave breaking field $E_{\text{br}} = 1.27 \times 10^{11} \text{ V m}^{-1}$; and the Langmuir period $T_L = 2\pi\omega_{pe0}^{-1} = 84.2 \text{ fs}$.) The combination of τ_L and n_{e0} yields $\hat{L} = 1$, the condition [24] that maximizes the amplitude of longitudinal electron velocity in the wake (11), $\hat{v}_{pz}^{\text{max}} = a_0^2 [\pi/(8e)]^{1/2} \approx 0.19$. The chosen plasma density defines the critical power for relativistic self-focusing, $P_{\text{cr}} = 16.2(1 - \varepsilon_L)^{-1} \text{ GW}$ [41], $P_{\text{cr}} = 16.2 \text{ TW}$. It also defines the frequency of the Cherenkov signal, $\nu = T_L^{-1} = 11.875 \text{ THz}$.

To display the spatial structure of the Cherenkov signal in figures 2 and 3, and to evaluate its amplitude in the wave zone in figure 4, we take the pulse with a waist size $\hat{r}_0 = 2\pi$ ($r_0 = 25.25 \mu\text{m}$). This defines the pulse energy (35), $W_{\text{laser}} \approx 0.36 \text{ J}$, and sets the lower bound (21) on emission angles,

$\theta_{Ch}^{\text{min}} \approx 8^\circ$. As dictated by equation (2), the pulse is marginally under-critical for relativistic self-focusing, $a_0 < a_{\text{cr}} = 0.9$ ($P/P_{\text{cr}} \approx 0.7$).

Figure 2 displays the magnetic field amplitudes within (14) and without the column (24). The stratification wave numbers are $\hat{K} = 1 - \sqrt{3}/2$ and $\hat{K} = 0.5$ ($\theta_{Ch} = 30^\circ$ and 60°). The shorter the stratification wavelength $2\pi\hat{K}^{-1}$, the larger the emission angle (20), the higher the free-space magnetic field. In addition, a thin column with the aspect ratio $\mathcal{R} = \hat{r}_0/\hat{R}_{\text{col}} = 1$ affords much higher free-space fields than a thick column with $\mathcal{R} < 1$.

Expressions (16) and (26) suggest that a transverse inhomogeneity of stratification ($\beta > 0$) should alter the free-space fields. This is demonstrated in figure 3. So long as the density grating amplitude varies weakly across the column ($\beta\hat{K} < 1$), the free-space field increases. Conversely, strong localization of the grating within the column, $\beta\hat{K} \gg 1$, suppresses the signal (this can be inferred from the structure of the integral (16), defining the amplitude of the free-space field.) As practical ways to control the homogeneity of stratification are as yet uncertain, we do not explore the matter further, concentrating on the study of THz signals emitted from homogeneously stratified columns.

Figure 4 displays the magnitude $\hat{E} = \langle \hat{\mathbf{E}}^{(\text{rad})} \cdot \hat{\mathbf{E}}^{(\text{rad})} \rangle^{1/2}$ of the electric field,

$$\hat{E} = 2^{-1/2} \alpha \hat{K} G_0 |C_H| \left[\hat{k}_{z-}^2 |H_1^{(1)}(\hat{k}_r r_{\perp})|^2 + \hat{k}_r^2 |H_0^{(1)}(\hat{k}_r r_{\perp})|^2 \right]^{1/2}, \quad (29)$$

as a function of emission angle within a range $\theta_{Ch}^{\text{min}} < \theta_{Ch} < 90^\circ$, for (1) $\mathcal{R} = 1$, (2) $\mathcal{R} = 2\pi^{-1}$, and (3) $\mathcal{R} = \pi^{-1}$. The field is sampled at a far-field distance $D = 10 \text{ cm}$ from the origin; the

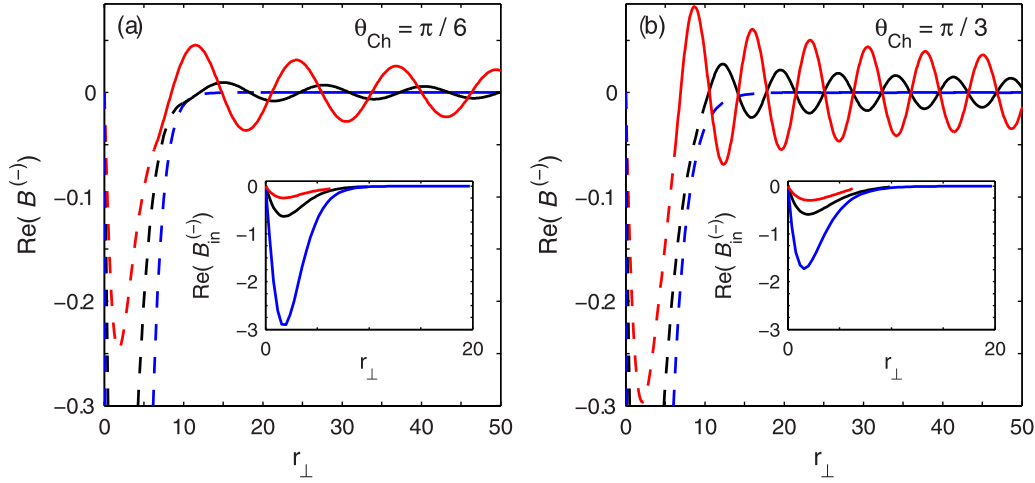


Figure 2. The free-space magnetic field (24) (solid curves in main panels) has the highest oscillation amplitude if the column radius matches the laser waist size, $\hat{R}_{\text{col}} = \hat{r}_0 = 2\pi$ (red); the amplitude falls as the column radius increases to $\pi\hat{r}_0/2$ (black), becoming almost negligibly small for $\hat{R}_{\text{col}} = \pi\hat{r}_0$ (blue.) Conversely, the field within the column (14) (dashed curves in main panels, solid in the insets) grows as the column radius increases. (Disparity in scales of main panels and insets emphasizes the difference in the field magnitude within and without the plasma.) The fields are shown for emission at (a) $\theta_{\text{Ch}} = 30^\circ$ and (b) 60° ; stratification is homogeneous, $\beta = 0$.

radial position of the detector is thus $D \sin \theta_{\text{Ch}} \approx 10$ cm for $\theta_{\text{Ch}} \approx 90^\circ$ and 1.4 cm for $\theta_{\text{Ch}}^{\text{min}} \approx 8^\circ$. (Remembering normalization, $r_{\perp} = \hat{D} \sin \theta_{\text{Ch}} \approx 2.5 \times 10^4 \sin \theta_{\text{Ch}}$ in equation (29).) In all three cases, the field magnitude rises sharply as the emission angle increases, reaching the MV m^{-1} -scale maximum at a right angle. The asymptotic approximation (40) for the near-forward emission, plotted in red, yields the electric field amplitude with a better than 10% accuracy for $\theta_{\text{Ch}} < 35^\circ$ ($\hat{K} < 0.175$). Except for $\theta_{\text{Ch}} \approx 90^\circ$, reduction in the aspect ratio \mathcal{R} suppresses the signal by orders of magnitude.

The thin column ($\mathcal{R} = 1$) appears to be the strongest emitter, the THz field strength varying from 28 kV m^{-1} to 3.8 MV m^{-1} in the wave zone ($D = 10$ cm, curve (1)). One can see that the THz signal frequency (11.875 THz) and its strength in the wave zone fully fit the requirements of experiments that could only be performed using a THz FEL [13]. Besides, the conical TM wave, sketched in figure 1, can be refocused using conical mirrors, reaching the field strength at the column surface (up to 240 MV m^{-1} , as shown in the inset in figure 4.) This is sufficient to drive the next generation of dielectric electron accelerators [20].

4.2. THz pulse power and radiation impedance

Equations (13) (where $\mathcal{B}^{(+)}$ is ignored, and $\mathcal{B}^{(-)} = \mathcal{B}_{\text{out}}^{(-)}$) and (22), with the complex field amplitudes (24) and (25), define the averaged over the Langmuir period energy flux density (the Poynting vector), $\langle \hat{\mathbf{S}} \rangle = (4\pi)^{-1} \langle \hat{\mathbf{E}}^{(\text{rad})} \times \hat{\mathbf{B}}^{(\text{rad})} \rangle = \hat{S}_{\infty} \hat{\mathbf{k}} + \Delta \hat{S} \hat{\mathbf{k}}_z - \mathbf{e}_z$, where

$$\hat{S}_{\infty} = \left(\frac{\alpha \hat{K} G_0 |C_H|}{2\pi} \right)^2 \frac{1}{\hat{k}_r r_{\perp}},$$

and $\Delta \hat{S} = \hat{S}_{\infty} \{ (\pi/2) [J_1^2(\hat{k}_r r_{\perp}) + Y_1^2(\hat{k}_r r_{\perp})] \hat{k}_r r_{\perp} - 1 \}$. Inequality (8.479.1) of [55] tells that $\Delta \hat{S} < (\hat{k}_r r_{\perp})^{-2} \hat{S}_{\infty}$ for $\hat{k}_r r_{\perp} > 1$.

The term $\Delta \hat{S}$ thus becomes small already at the column surface, provided that \hat{R}_{col} is sufficiently large, and the Cherenkov angle not too small, so that $\hat{k}_r r_{\perp} \approx w > 1$. The Poynting vector in the wave zone thus reads

$$\langle \hat{\mathbf{S}}(r_{\perp} \gg \hat{k}_r^{-1}) \rangle = \hat{S}_{\infty} \hat{\mathbf{k}}. \quad (30)$$

(Using the field asymptotic (27) and (28) yields, naturally, the same result.) For any emission point within the interval $0 \leq z \leq \hat{L}_{\text{pl}}$, the Poynting vector (30) is directed along the same wave vector $\hat{\mathbf{k}}$, as sketched in figure 1. Encompassing the plasma column with a sufficiently long coaxial cylinder of a large radius ($\gg \hat{k}_r^{-1}$), it is easy to see that all emitted energy flows through the lateral surface of the cylinder, through the segment with the length equal to the plasma length \hat{L}_{pl} . Integrating the radial component of flux (30) over the surface of this segment yields a time-averaged emission power,

$$\hat{P} = \oint_S \langle \hat{\mathbf{S}} \rangle \cdot \mathbf{ds} = (a_0/2)^4 \hat{L}^2 e^{-\hat{L}^2} (\alpha \hat{K} |C_H|)^2 \hat{L}_{\text{pl}}. \quad (31)$$

The plasma cylinder of a radius \hat{R}_{col} and a length \hat{L}_{pl} contains the laser wake energy (37). Cherenkov emission drains it at a rate $\hat{\gamma} \equiv \hat{T}^{-1}$. This energy loss may be referred to as the ‘radiation impedance.’ Assuming that the energy loss per unit time (in physical units, per $\omega_{\text{pe}0}^{-1} \approx 1.77 \times 10^{-5} n_{e0}^{-1/2} [\text{cm}^{-3}] \text{ s}$) is small, the depletion time may be estimated using the energy balance equation [39], $\hat{P} = -\partial/\partial t (\int_V \hat{U} \text{d}\mathbf{r}) \approx \hat{T}^{-1} \hat{W}_{\text{wake}}$, with the energy density \hat{U} and initial energy supply \hat{W}_{wake} given by formulae (36) and (37):

$$\begin{aligned} \hat{T} &= \frac{\hat{W}_{\text{wake}}}{\hat{P}} \\ &\approx \frac{\pi \hat{r}_0^2}{(4\alpha \hat{K} |C_H|)^2} \left\{ 1 + (2/\hat{r}_0)^2 - e^{-u^2} [1 + (2/\hat{r}_0)^2 (1 + u^2)] \right\}. \end{aligned} \quad (32)$$

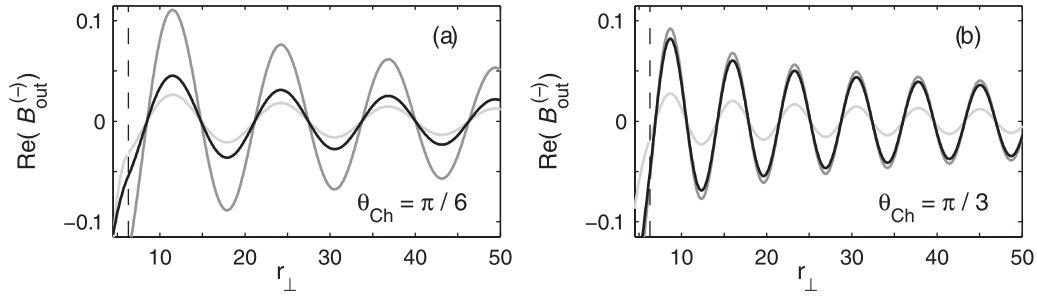


Figure 3. Transverse inhomogeneity of stratification ($\beta > 0$) alters the free-space magnetic field (24). As in figure 2, the emission angle (a) $\theta_{\text{Ch}} = 30^\circ$ and (b) 60° . The column radius matches the laser waist size, $\hat{R}_{\text{col}} = \hat{r}_0 = 2\pi$, a vertical dashed line marking the border of the column. A weakly non-uniform stratification ($\beta\hat{K} = 0.5$, gray curves) increases the signal, most considerably for the forward emission (panel (a)). Strong inhomogeneity ($\beta\hat{K} = 5$, light gray) suppresses the signal. Black curves (identical to the red curves of figure 2) correspond to homogeneous stratification, $\beta = 0$.

Here, $u = 2\mathcal{R}^{-1} > 1$. The depletion time $\hat{T}(\hat{r}_0, \hat{R}_{\text{col}})$ is defined entirely by the geometry of the system (i.e. by the laser pulse waist size and the column radius), and is thus a natural figure of merit for the energy transfer from the electrostatic Langmuir mode to the free-space TM mode (the shorter the \hat{T} , the more efficient mode conversion.)

4.3. Energy conversion: from optical to THz

The wake lifetime defines the duration of Cherenkov signal. Phase mixing of electron oscillations over the density gradient (longitudinal wave breaking) [42, 43] destroys the wake much sooner than the Cherenkov emission depletes it. Assuming weak stratification and using equation (7) of paper [43], we find that a small-amplitude, quasi-1D Langmuir wave breaks within an interval (normalized to the Langmuir period T_L)

$$\hat{T}_{\text{br}} \approx [\pi G_0 |\partial n / \partial z|_{\text{max}}]^{-1} \leq (2\alpha a_0^2 \hat{K} \hat{L})^{-1} e^{\hat{L}^2/2}. \quad (33)$$

The regime specified in section 4.1 corresponds to $\hat{T}_{\text{br}} \approx 17\hat{K}^{-1}$. The plasma wave (hence, the THz signal) thus lasts at least a few tens of Langmuir periods. With $T_L \approx 84$ fs, the wake lifetime $T_{\text{br}} \approx 1.4$ ps for $\hat{K} \rightarrow 1$ and 140 ps for $\hat{K} \approx 0.01$. (Incidentally, it takes about as long for the ions to respond to the ponderomotive force of the radially non-uniform wake, and to break the wake transversely [49]; or for the ions to start diffusing into the ambient gas, dissipating the column [47, 48].)

Knowing the emission duration (33), we evaluate the efficiency of energy conversion from optical to THz, $\eta = PT_{\text{br}}/W_{\text{laser}}$, another important metric of the signal. Here, the THz signal power, its length, and the total energy of the drive laser pulse are in Watts, seconds, and Joules, respectively. Expressing the efficiency through the normalized quantities (31), (33), and (35), we arrive at a formula $\eta = U\hat{P}\hat{T}_{\text{br}}/\hat{W}_{\text{laser}}$ with a unit conversion factor $U = 2\pi c \varepsilon_0 (\lambda_0 E_{\text{br}})^2 W_0^{-1}$. Here, the speed of light $c = 3 \times 10^8$ m s^{-1} ; the dielectric permittivity of free space $\varepsilon_0 = 8.85 \times 10^{-12}$ F m^{-1} ; the laser wavelength λ_0 is in meters; E_{br} is in V m^{-1} ; and $W_0 \approx 1.4 \times 10^{10}$ W. With the plasma length close to the Rayleigh length, the conversion efficiency reads

$$\eta(\hat{Z}_R) \approx 4 \times 10^{-3} U (1 - \varepsilon_L)^{-1/2} e^{-\hat{L}^2/2} \alpha \hat{K} |C_H|^2. \quad (34)$$

This expression may be converted into a form convenient for applications,

$$\eta(\hat{Z}_R) \approx 1.5 \times 10^{-12} \lambda_0 [\mu\text{m}] n_{e0}^{1/2} [\text{cm}^{-3}] e^{-\hat{L}^2/2} \alpha \hat{K} |C_H|^2.$$

Similarly to the wake depletion time (32), the efficiency (34) is independent of the drive pulse amplitude. Hence, so long as the aspect ratio \mathcal{R} is fixed, the efficiency depends solely on the laser pulse length and waist size.

The trends demonstrated in figures 2 and 4 are supported by the study of THz generation efficiency in figure 5, for the same set of physical parameters. The efficiency is characterized in terms of both wake depletion time (32) (figure 5(a)) and the energy conversion efficiency (34) (figure 5(c)). One can see a rapid increase in efficiency with the increase in emission angle, and a sharp decline with the reduction in the aspect ratio \mathcal{R} . The power of the signal (31) (figure 5(b)) follows the same trends, the signal with the highest power (≈ 5 MW) emitted at a right angle from the thin column ($\mathcal{R} = 1$).

Figure 5(a) points out that Cherenkov emission depletes the wake negligibly. For any given emission angle exceeding $\theta_{\text{Ch}}^{\text{min}} \approx 8^\circ$ (21), the wake depletion time (32) remains about two orders of magnitude longer than the wake lifetime (33) (the THz signal length). The conversion efficiency (34) thus remains modest, yet comparable with other laser plasma-based methods of THz generation [4]. From figure 5(c), the highest efficiency 2×10^{-5} corresponds to emission of a 7 μJ THz signal at a right angle.

Concluding the section, we explore the scaling of conversion efficiency (34) with the laser wavelength and background plasma density. Recalling $\hat{K} |C_H|^2 \sim n_{e0}^{1/2}$ and $\hat{L} \sim n_{e0}^{1/2}$, we find $\eta \sim \lambda_0 (n_{e0}/n_{e0}^{(0)}) e^{-(n_{e0}/n_{e0}^{(0)})/2}$, where the constant $n_{e0}^{(0)} \approx 1.74 \times 10^{21} \tau_L^{-2} [\text{fs}] \text{cm}^{-3}$ is the resonant density that yields $\hat{L} = 1$. So long as the mean background density n_{e0} and the drive pulse length τ_L are fixed, the efficiency increases proportionally to the laser wavelength. This favors driving the wake with short-pulse, mid-infrared lasers [44, 45]. Conversely, if the wavelength is constant, the efficiency is the highest around $n_{e0} \approx 2n_{e0}^{(0)}$, tending to zero as n_{e0} deviates from this optimal value. As a reminder, the drive pulse in both scenarios must remain non-relativistic

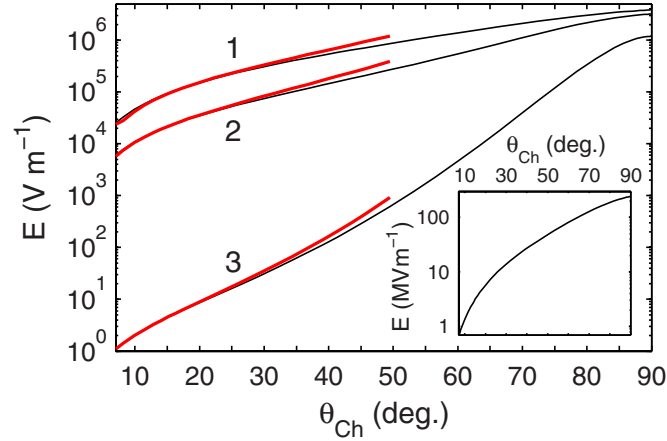


Figure 4. Electric field amplitude (29) (black), sampled at a 10 cm distance from the origin, grows as the emission angle increases (the stratification wavelength decreases), and falls as the aspect ratio drops from (1) $\mathcal{R}=1$ to (2) $2\pi^{-1}$ to (3) π^{-1} . Physical parameters are those of figure 2. The forward emission asymptotic (40) is plotted in red. Inset shows electric field (29) in the case (1), at the column surface ($r_{\perp} = \hat{R}_{\text{col}}$).

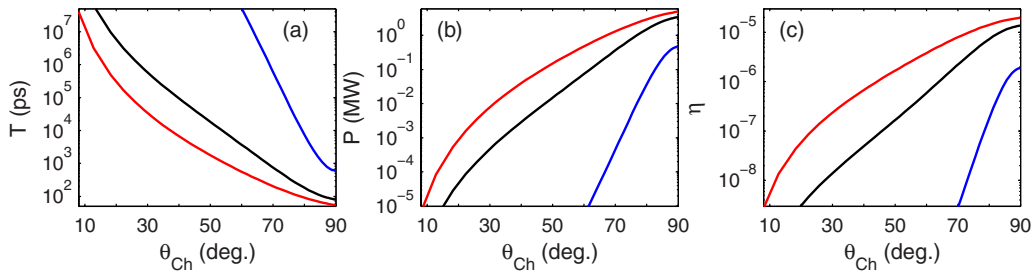


Figure 5. (a) The wake depletes faster as the emission angle increases, and as the aspect ratio approaches unity (blue: $\mathcal{R} = \pi^{-1}$; black: $\mathcal{R} = 2\pi^{-1}$; red: $\mathcal{R} = 1$; as in figure 2, $\hat{r}_0 = 2\pi$). The depletion time (32) exceeds 50 ps. (b) Power (31) of the THz signal and (c) the energy conversion efficiency (34) both increase with the angle and rapidly decline with the reduction in the aspect ratio.

and sub-critical for the relativistic self-focusing, meeting the condition (3).

5. Trends in energy conversion efficiency

The study of a similar system in a Cartesian, planar 2D geometry, for the parameters close to those defined in section 4.1, concludes that conversion of the electromagnetic energy, from optical to THz, depends rather weakly on the aspect ratio, even for $\mathcal{R} \approx 0.5$ remaining optimistically high, $\eta \approx 2 \times 10^{-4}$.

Our figures 2–5 bear evidence to the contrary, showing a rapid decline in the THz generation efficiency as \mathcal{R} drops below unity. Furthermore, the maximum value of efficiency (cf figure 5(c)) is an order of magnitude lower than earlier reported. This section further supports this message, examining changes in the emission metrics brought forth by varying the drive pulse power. We consider oblique ($\theta_{\text{Ch}} = 45^\circ$, $\hat{K} = 1 - 2^{-1/2}$) and orthogonal emission ($\theta_{\text{Ch}} = 90^\circ$, $\hat{K} \rightarrow 1$), for a range of laser waist sizes and column radii, keeping the laser peak intensity fixed ($a_0 = 0.7$, as defined in section 4.1). The THz signal length is thus $T_{\text{br}} \approx 4.85$ ps for the oblique emission (56 Langmuir cycles), and 1.4 ps for the orthogonal one (17 cycles.) It appears that the aspect ratio $\mathcal{R} \approx 1$

remains optimal in this setting as well, with an about 20% accuracy.

Figure 6 presents the results of a first set of scans, in which we compare three cases with fixed drive pulse parameters. The three pulses are chosen with the waist sizes $\hat{r}_0^{(1)} = 2e^{-1/2}$ ($r_0 \approx 4.9 \mu\text{m}$), $\hat{r}_0^{(2)} = \pi$ ($r_0 \approx 12.6 \mu\text{m}$), and, as in section 4, $\hat{r}_0^{(3)} = 2\pi$ ($r_0 \approx 25.25 \mu\text{m}$). The pulse energy (power ratio P/P_{cr}) is thus, respectively, 13.3 mJ (0.026), 90 mJ (0.18), and 0.36 J (0.7). The energy supply for emission — the wake energy (37) contained in the column with $\mathcal{R} \approx 1$ — is, respectively, 1.2 μJ , 21 μJ , and 0.26 mJ. In each case, we vary the column radius \hat{R}_{col} , exploring the dependence of efficiency (34) on the aspect ratio \mathcal{R} .

In the case of oblique emission ($\theta_{\text{Ch}} = 45^\circ$, figure 6(a)), the higher the drive pulse power (i.e. the larger the waist size), the stronger the falloff in efficiency caused by the reduction in the aspect ratio. As $\mathcal{R} \rightarrow 0.5$, the efficiency drops from its maximum merely by half for $\hat{r}_0 = \hat{r}_0^{(1)}$; by a factor 19.5 for $\hat{r}_0 = \hat{r}_0^{(2)}$; and by a factor 320 for $\hat{r}_0 = \hat{r}_0^{(3)}$. This dramatic (in fact, exponential) decline may be deduced from the asymptotic (43).

Figure 6(a) also indicates that the peak in efficiency grows slowly so long as the pulse is weakly focused (i.e. from $\eta_{\text{max}} = 1.11 \times 10^{-6}$ to 1.25×10^{-6} , as the waist size \hat{r}_0 doubles, from π to 2π .) The peak shifts to a 50% larger aspect ratio, from

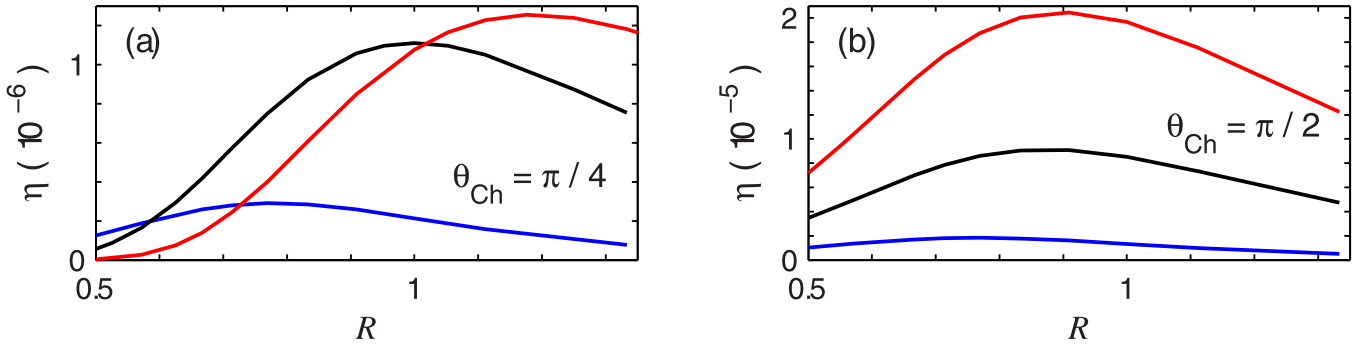


Figure 6. The drive pulse amplitude being constant, $a_0 = 0.7$, the efficiency of emission (34) at both (a) $\theta_{Ch} = 45^\circ$ and (b) 90° is the highest for the aspect ratio $\mathcal{R} = 1 \pm 0.2$ (note the difference in vertical axes scales.) As the driver waist size (energy) rises from $\hat{r}_0 = 2e^{-1/2}$ (13.3 mJ; blue) to π (90 mJ; black) to 2π (0.36 J; red), the peak efficiency increases. If the pulse is weakly focused, $\hat{r}_0 \geq \pi$, the efficiency of emission at 45° sharply falls as $\mathcal{R} \rightarrow 0.5$, in contrast to steadier variation at $\theta_{Ch} = 90^\circ$.

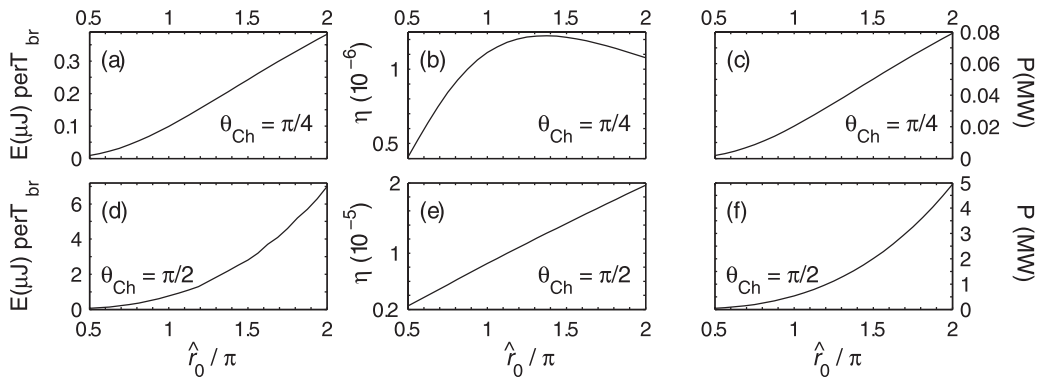


Figure 7. With the optimal aspect ratio ($\mathcal{R} = 1$) and the drive pulse amplitude fixed ($a_0 = 0.7$), the energy of the THz signal ((a), (d)) and its power ((c), (f)) grow monotonously as the drive pulse waist size (i.e. its power) increases. The top row corresponds to the lateral ($\theta_{Ch} = 45^\circ$), and the bottom row to the orthogonal emission (90°). The efficiency of lateral emission (panel (b)) nearly saturates for $\hat{r}_0 > \pi$, whereas the efficiency of orthogonal emission increases linearly (panel (e)).

$\mathcal{R} = 0.77$ to 1.175 , as the waist size increases 5-fold, from $\hat{r}_0^{(1)}$ to $\hat{r}_0^{(3)}$.

Emission at a right angle (figure 6(b)) reveals somewhat different trends. First, the dependence of efficiency on the aspect ratio is weaker, η falling by less than a factor 2.85 for all three cases as $\mathcal{R} \rightarrow 0.5$. This can be deduced from the power-law asymptotic (44) (as opposed to the exponential asymptotic (43) for the lateral emission.) Secondly, the efficiency peak does not drift toward larger aspect ratios, staying at $\mathcal{R} = 0.9$ for $\hat{r}_0 \geq \pi$. Thirdly, the peak efficiency does not saturate as the pulse power (the waist size) grows.

Figure 7 shows variation in emission metrics as the drive pulse waist size and the column radius vary together, remaining matched, $\mathcal{R} = 1$. Similarly to the trend in figure 6(a), the efficiency of oblique emission (figure 7(b)) almost saturates for $\hat{r}_0 > \pi$; in contrast, the efficiency of orthogonal emission (figure 7(e)) grows linearly with the waist size. The pulse with a constant peak intensity deposits more energy into the wake as its waist size (hence, the volume of the radiating plasma) increases. As a result, the THz signal energy ((a), (d)) and power ((c), (f)) grow steadily as the drive pulse waist increases, showing no sign of saturation as the pulse becomes near-critical for relativistic self-focusing. (As the self-focusing threshold is crossed, the collapsing driver

shall promptly cavitate the wake [58], completely altering the emission pattern; exploring these fully non-linear transient dynamics in particle-in-cell simulations is a subject of another paper.) The highest values of the conversion efficiency ($\eta = 2 \times 10^{-5}$), the THz pulse power (≈ 5 MW), and total emitted energy ($\approx 7 \mu\text{J}$) correspond to the orthogonal emission from the wake driven by a marginally sub-critical driver, $\hat{r}_0 = 2\pi$ ($P/P_{cr} \approx 0.7$).

6. Summary and outlook

Conversion, in the nonhomogeneous plasmas, of electrostatic Langmuir waves into electromagnetic waves is a fundamental issue with a long history [59–62]. Rotational currents, driven in the plasmas by the ponderomotive force of a short, intense laser pulse (partly pertaining to the pulse-driven 3D Langmuir waves—laser wakes [24]), are in the THz frequency range [1, 2, 7, 8, 35–38]. There is a concerted effort of using these currents as a basis of plasma based, short-pulse THz radiation sources [4]. THz radiation from the laser plasmas is ubiquitous. However, the existing scenarios, such as those involving plasma filaments [5, 6], ponderomotively-driven

currents in the longitudinally stratified yet radially homogeneous plasmas [1], corrugated leaky channels [2], or laser-solid interactions [63], reveal extremely short-pulsed (down to a single cycle), broadband THz emission with a large angular dispersion. Generating a multi-cycle *monochromatic*, coherent THz signal still remains a technical challenge, partly because clear understanding of the underlying mechanisms is wanting.

The observation that the plasma current begetting such a signal must be monochromatic and coherent disqualifies the electron flow surrounding the laser pulse. This flow is driven by the ponderomotive push, which lasts shorter than a Langmuir period. The pulsed excitation, taking shorter than a single THz cycle, makes for a broadband signal [1]. Mode conversion within sharp density gradients (such as ionization fronts) is also out of question, as the bandwidth of the THz pulse is defined in this case by the jump in the background plasma density, and is thus of the order of the mean signal frequency [35]. Conversely, as is clear from equations (10) and (11), electron velocity oscillations in the laser wake remain almost monochromatic if the plasma is weakly stratified. Coupling this electron velocity to the slowly varying gradient in the background density [1] offers a physical solution to the problem of monochromatic THz emission.

In the physical system, the drive pulse passes a certain point in the plasma, upsetting a charge neutrality (the ions remain at rest.) The electron velocity starts oscillating at the Langmuir frequency. Coupling the velocity of transverse electron oscillations to the longitudinal gradient of the background density generates the low-frequency azimuthal rotational current (also oscillating at the Langmuir frequency.) Periodic stratification of the plasma increases the current wavelength, making the current superluminal. *If the plasma is radially bounded*, the superluminal current emits a Cherenkov signal (a conical TM wave), monochromatic at the Langmuir frequency. This emission from periodically (spatially) modulated currents, driven by an external source in the bounded medium, was first described by Smith and Purcell [40]. The lifetime of the wake (hence, the duration of the THz signal) is limited by wave breaking in the inhomogeneous plasma [42, 49]. The effect, depending on the wake amplitude, stratification parameters, and the radial extent of the wake, limits the signal length to a few hundreds of Langmuir cycles (tens of picoseconds.)

We have found that maximizing the wake-driven magnetic field at the border of the column, as defined by the integration constant (26), increases the signal. To this end, the column radius must be close to the waist size of the drive pulse. Even in this optimal scenario, Cherenkov emission depletes the wake weakly. The energy conversion, from optical to THz, remains on the level of 10^{-6} for the emission at 45° , rising to 10^{-5} for the emission at a right angle. This may look modest compared with the recent reports on energy conversion in the air filaments [6]. However, due to its monochromaticity, the signal from the laser wake is clearly competitive in terms of spectral brightness (i.e. the energy in the small spectral interval around the carrier frequency ω_{pe0} .) In

addition, working slightly under the threshold of relativistic self-focusing maximizes all signal metrics (its energy, power, and conversion efficiency.) As a bonus, the relativistic Kerr effect will partly suppress the drive pulse diffraction, extending the plasma column length to several Rayleigh lengths without external waveguide. Lastly, the conversion efficiency tends to increase with the wavelength of the drive pulse, which opens the field for application of high-power, short-pulse mid-infrared lasers [44, 45].

Imprinting an ion density grating, with a spatial period under $100 \mu\text{m}$, into a cm-scale laser plasma is technically non-trivial. One may seek an alternative, in switching from periodically stratified to density-tapered targets [65], with the density of gas gradually increasing along the drive pulse path. In the following papers, we shall examine this opportunity using the developed theoretical framework.

Acknowledgment

The work is supported by the AFRL contracts FA9451-17-F-0011 and FA9451-20-F-0001, and AFOSR grants FA9550-16RDCOR325, FA9550-19RDCOR023, and FA9550-19RDCOR027. Approved for public release; distribution is unlimited. Public Affairs release approval AFMC-2020-0264.

Appendix A. Energy stored in laser wake

The Gaussian laser pulse with the peak intensity I_{max} , length L , and waist size r_0 contains the energy [64] $W_{\text{laser}} = (2\pi)^{-2} (1 - \varepsilon_L)^{-1} (W_0/\omega_{pe0}) \hat{W}_{\text{laser}}$, where $W_0 \approx 1.4 \times 10^{10} \text{ W}$, and

$$\hat{W}_{\text{laser}} = (\pi^3/2)^{1/2} (a_0 \hat{r}_0)^2 \hat{L}. \quad (35)$$

Part of this energy, W_{wake} , is imparted into the wake field.

The cylindrical Langmuir wave, excited in the plasma column of a radius R_{col} and length L_{pl} , is the energy reservoir for electromagnetic emission. How much energy the drive pulse imparts into the wake as it swipes the plasma of a length L_{pl} may be estimated from the wave energy balance [24]. An equally accurate estimate may be obtained from calculating the energy density of the wake [39]:

$$\hat{U} = (8\pi)^{-1} d(\hat{\omega}\varepsilon)/d\hat{\omega} \langle \hat{\mathbf{E}}_{EPW}^2 \rangle = (8\pi)^{-1} (\hat{E}_{0r}^2 + \hat{E}_{0z}^2). \quad (36)$$

The angular brackets mean averaging over the Langmuir period; the derivative of the dielectric permittivity, $\varepsilon = 1 - \hat{\omega}^{-2}$, is evaluated near the Langmuir frequency $\hat{\omega} = 1$; and

$$\begin{aligned} \hat{E}_{0r} &= -(\pi/8)^{1/2} a_0^2 \hat{L} e^{-\hat{L}^2/2} (4r_\perp/\hat{r}_0^2) e^{-2r_\perp^2/\hat{r}_0^2} \\ \hat{E}_{0z} &= (\pi/8)^{1/2} a_0^2 \hat{L} e^{-\hat{L}^2/2} e^{-2r_\perp^2/\hat{r}_0^2} \end{aligned}$$

are the familiar amplitudes of radial and longitudinal electrostatic fields [24], normalized to the cold wave breaking field E_{br} . Integrating (36) over the volume of the plasma cylinder yields the total (normalized) wake energy,

$$\hat{W}_{\text{wake}} = \hat{V}(a_0/4)^4 \hat{L}^2 e^{-L^2} \left\{ 1 + (2/\hat{r}_0)^2 - e^{-u^2} [1 + (2/\hat{r}_0)^2 (1 + u^2)] \right\}, \quad (37)$$

where $\hat{V} = \pi \hat{r}_0^2 \hat{L}_{\text{pl}}$, and $u = 2\mathcal{R}^{-1} > 1$. Wake energy in Joules $W_{\text{wake}} = \varepsilon_0 k_{\text{p}0}^{-3} E_{\text{br}}^2 \hat{W}_{\text{wake}}$, where the dielectric permittivity of free space $\varepsilon_0 = 8.85 \times 10^{-12}$ F m⁻¹; $k_{\text{p}0} = 1.88 \times 10^{-4} n_{\text{e}0}^{1/2}$ [cm⁻³] m⁻¹; and E_{br} is in V m⁻¹.

Appendix B. Asymptotic of low-frequency magnetic field in transversely homogeneous plasma

Consider the driven solution for the magnetic field (15) with $\hat{R}_{\text{col}} = \infty$, starting with its second term. As $r_{\perp} \rightarrow \infty$, $K_1(\hat{k}_{z\pm}s) \rightarrow [\pi/(2\hat{k}_{z\pm}s)]^{1/2} e^{-\hat{k}_{z\pm}s} < [\pi/(2\hat{k}_{z\pm}s)]^{1/2}$ in the integral (17). Hence, per identity (3.381.3) of [55], this integral is bound from above as $\mathcal{I}_K^{\pm}(\infty, r_{\perp} \rightarrow \infty) < [\pi \hat{r}_0 / (2\hat{k}_{z\pm})]^{1/2} [2(1 + \beta \hat{K})]^{-5/4} \Gamma(5/4, b)$, where Γ is the incomplete gamma function of the argument $b = 2(1 + \beta \hat{K})(r_{\perp}/\hat{r}_0)^2$. For large b , the asymptotic (8.357.1) of [55] yields $\Gamma(5/4, b) \approx b^{1/4} e^{-b}$; hence, $\mathcal{I}_K^{\pm}(\infty, r_{\perp} \rightarrow \infty) < [\pi r_{\perp} / (2\hat{k}_{z\pm})]^{1/2} [2(1 + \beta \hat{K})]^{-1} e^{-2(1 + \beta \hat{K})(r_{\perp}/\hat{r}_0)^2}$. Remembering that $I_1(\hat{k}_{z\pm} r_{\perp}) \sim (2\pi \hat{k}_{z\pm} r_{\perp})^{-1/2} e^{\hat{k}_{z\pm} r_{\perp}}$ for large values of the argument, we find that the second term in equation (15) decays very rapidly for $r_{\perp} > \hat{k}_{z\pm} \hat{r}_0^2 [2(1 + \beta \hat{K})]^{-1}$,

$$I_1(\hat{k}_{z\pm} r_{\perp}) \mathcal{I}_K^{\pm}(\infty, r_{\perp}) < [4\hat{k}_{z\pm}(1 + \beta \hat{K})]^{-1} e^{-2(1 + \beta \hat{K})(r_{\perp}/\hat{r}_0)^2},$$

and may be thus ignored. Regarding the first term in equation (15), the identities (6.643.2), (9.220.2), and (9.215.1) of [55] yield the asymptotic

$$\mathcal{I}_I^{\pm}(r_{\perp} \rightarrow \infty) \rightarrow [\hat{k}_{z\pm}(1 + \beta \hat{K})]^{-1} u_{\pm} e^{u_{\pm}}, \quad (38)$$

where $u_{\pm} = (\hat{k}_{z\pm} \hat{r}_0)^2 [8(1 + \beta \hat{K})]^{-1}$. Finally, the asymptotic of $K_1(\hat{k}_{z\pm} r_{\perp})$ at large values of the argument yields the exponentially evanescent at infinity magnetic field (23).

Appendix C. Forward Cherenkov emission: asymptotic for C_H

Analytical estimates for the constant (26), defining the radiation vector fields (27) and (28), are possible for the emission in the forward direction, such as $\hat{K} < 0.1$ (or $\theta_{\text{Ch}} < 25^\circ$), and $\hat{R}_{\text{col}} \gg 1$. In this case, $v \gg 1$, $w \sim 1$, and, with a precision better than 10%,

$$|C_H|^2 \approx \frac{\mathcal{F}}{(\pi w/2)[J_1^2(w) + Y_1^2(w)]}. \quad (39)$$

Here, $\mathcal{F} = (1 + \varepsilon_L^{-1/2} \beta)^2 [\pi \mathcal{I}_I^-(\hat{R}_{\text{col}}) e^{-v}]^2 \tan \theta_{\text{Ch}}$, and $\tan \theta_{\text{Ch}} \equiv \hat{k}_r / \hat{k}_{z-} = w/v$. So long as $w > 1$, the identity (8.479.1) of [55] bounds $|C_H|^2$ to the interval

$$\mathcal{F} \sqrt{1 - w^{-2}} < |C_H|^2 \leq \mathcal{F}. \quad (40)$$

From the definition (19), the condition $w > 1$ implies $\hat{K} > (2\hat{R}_{\text{col}}^2)^{-1}$. So long as $\hat{R}_{\text{col}} \sim \hat{r}_0^2$, and $\hat{r}_0 > \pi$, the approximation (40) works for $K > 5 \times 10^{-3}$, hence the range of the emission angles $6^\circ < \theta_{\text{Ch}} < 25^\circ$. In this near-forward range, where $\hat{K} \sim \theta_{\text{Ch}}^2$, the definition of \mathcal{F} suggests $(\hat{K}|C_H|)^2 \sim \mathcal{O}(\theta_{\text{Ch}}^5)$, so that the radial energy flux $\langle S_r \rangle$ (cf equation (30)) changes with the emission angle rather sharply.

In the limit $w \ll 1$, or $\hat{K} \ll (2\hat{R}_{\text{col}}^2)^{-1}$ (emission almost in the forward direction), equation (39) reduces to $|C_H|^2 \approx (\pi w/2) \mathcal{F}$. With $w \approx \theta_{\text{Ch}}$, we have $\langle S_r \rangle \sim \mathcal{O}(\theta_{\text{Ch}}^6)$.

Finally, if $\hat{r}_0 > \pi$, and $\mathcal{R} < [\pi(1 + \beta \hat{K}) / (2\hat{r}_0)]^{1/2}$, expression for \mathcal{F} may be further simplified using equation (38), $\mathcal{I}_I^-(\hat{R}_{\text{col}}) \approx \mathcal{I}_I^-(\infty)$. The overestimation is less than 20%.

Appendix D. Lateral Cherenkov emission: asymptotic for C_H

For the oblique emission, such as neither $v = \hat{k}_{z-} \hat{R}_{\text{col}}$ nor $w = \hat{k}_r \hat{R}_{\text{col}}$ is vanishing, and, besides, $v > 1$, one has $I_0(v) \approx I_1(v) \approx (2\pi v)^{-1/2} e^v$. Then, for $\hat{r}_0 > \pi$, and $\mathcal{R} < [\pi(1 + \beta \hat{K}) / (2\hat{r}_0)]^{1/2}$, so that the estimate $\mathcal{I}_I^-(\hat{R}_{\text{col}}) \approx \mathcal{I}_I^-(\infty)$ holds, one finds

$$C_H \approx \frac{(2\pi)^{1/2} (1 + \beta)(1 + \beta \hat{K})^{-1}}{H_0^{(1)}(w) \tan \theta_{\text{Ch}} - H_1^{(1)}(w)} v^{-1/2} e^{-v} u_- e^{u_-}. \quad (41)$$

So long as w is not small, the denominator in equation (41) is of the order unity. The factor $u_- e^{u_-}$ then defines the asymptotic behavior of C_H as the laser waist size changes and the column radius remains fixed. Conversely, the factor $v^{-1/2} e^{-v}$ defines the C_H asymptotic as the column radius changes, while the laser waist size is fixed (as in figure 6.) In the former case, as soon as $\mathcal{R} < 8v^{-1}(1 + \beta \hat{K})$, expression (41) reduces to

$$C_H(\mathcal{R} \rightarrow 0) \approx \left(\frac{\pi}{32} \right)^{1/2} \frac{(1 + \beta)(1 + \beta \hat{K})^{-2} v^{3/2} e^{-v}}{H_0^{(1)}(w) \tan \theta_{\text{Ch}} - H_1^{(1)}(w)} \mathcal{R}^2. \quad (42)$$

(Only \mathcal{R} varies in the asymptotic (42), while v and w are constants.) In the latter case (when u_- is constant), the asymptotic reads

$$C_H(\mathcal{R} \rightarrow 0) \approx \left(\frac{\pi^2}{2} \right)^{1/4} \frac{(1 + \beta)(1 + \beta \hat{K})^{-5/4} u_-^{3/4} e^{u_-}}{H_0^{(1)}(w) \tan \theta_{\text{Ch}} - H_1^{(1)}(w)} \mathcal{R}^{1/2} e^{-\kappa_u \mathcal{R}^{-1}}, \quad (43)$$

where $\kappa_u = [8(1 + \beta \hat{K}) u_-]^{1/2} = \hat{k}_{z-} \hat{r}_0 > 1$. In either case, as soon as $\hat{r}_0 > \pi$, and the aspect ratio drops, the decline in the integration constant C_H dictates a rapid decline in the signal amplitude. This explains the trend depicted in figure 6(a).

As regards emission at a right angle, it corresponds to $v \rightarrow 0$, and $w \rightarrow \hat{R}_{\text{col}}$. In this case, $v I_0(v) \approx 2I_1(v) \approx \hat{k}_{z-} \hat{R}_{\text{col}}$.

Then, within the range of validity of the estimate $\mathcal{I}_I^-(\hat{R}_{\text{col}}) \approx \mathcal{I}_I^-(\infty) \approx [8(1+\beta\hat{K})]^{-1} \hat{k}_z - \hat{r}_0^2$, one finds

$$C_H(\mathcal{R} \rightarrow 0) \approx \frac{(1+\beta)(1+\beta\hat{K})^{-2}(\mathcal{R}/2)^2}{H_0^{(1)}(\hat{R}_{\text{col}}) - 2\hat{R}_{\text{col}}^{-1}H_1^{(1)}(\hat{R}_{\text{col}})} \sim \mathcal{O}(\mathcal{R}^2). \quad (44)$$

ORCID iD

Serge Kalmykov  <https://orcid.org/0000-0002-0946-857X>

References

- [1] Gorbunov L M and Frolov A A 1996 *JETP* **83** 967–73
- [2] Miao C, Palastro J P and Antonsen T M Jr. 2017 *Phys. Plasmas* **24** 043109
- [3] Kamphrath T, Tanaka K and Nelson K A 2013 *Nat. Photon.* **7** 680–90
- [4] Fülöp J A, Tzortzakis S and Kamphrath T 2019 *Adv. Opt. Mater.* **8** 1900681
- [5] González de Alaiza Martínez P, Davoine X, Debayle A, Gremillet L and Bergé L 2016 *Sci. Rep.* **6** 26743
- [6] Koulouklidis A D, Gollner C, Shumakova V, Fedorov V Y, Pugžlys A, Baltuška A and Tzortzakis S 2020 *Nat. Commun.* **11** 292
- [7] Sprangle P, Peñano J R, Hafizi B and Kapetanacos C A 2004 *Phys. Rev. E* **69** 066415
- [8] Volchok E P, Timofeev I V and Annenkov V V 2019 *Plasma Phys. Control. Fusion* **61** 125006
- [9] Elias R L, Hu J and Ramian G 1985 *Nucl. Instrum. Methods Phys. Res. A* **237** 203–6
- [10] Knippels G M H, Mols R F X A M, van der Meer A F G, Oepets D and van Amersfoort P W 1995 *Phys. Rev. Lett.* **75** 1755–8
- [11] Gensch M et al 2008 *Infrared Phys. Technol.* **51** 423–5
- [12] Zvyagin S A, Ozerov M, Čížmár E, Kamenskyi D, Zherlitsyn S, Herrmannsdörfer T, Wosnitza J, Wunsch R and Seidel W 2009 *Rev. Sci. Instrum.* **80** 073102
- [13] Wagner M, Schneider H, Stehr D, Winner S, Andrews A M, Schartner S, Strasser G and Helm M 2010 *Phys. Rev. Lett.* **105** 167401
- [14] Greenland P T, Lynch S A, van der Meer A F G, Murdin B N, Pidgeon C R, Redlich B, Vinh N Q and Aeppli G 2010 *Nature* **465** 1057–61
- [15] Dienst A et al 2013 *Nat. Mater.* **12** 535–41
- [16] Liu J and Zhang X C 2009 *Phys. Rev. Lett.* **103** 235002
- [17] Clough B, Dai J and Zhang X C 2012 *Mater. Today* **15** 50–8
- [18] Wen H, Wiczer M and Lindenberg A M 2008 *Phys. Rev. B* **78** 125203
- [19] Hoffmann M C, Hebling J, Hwang H Y, Yeh K L and Nelson K A 2009 *Phys. Rev. B* **79** 161201(R)
- [20] Nanni E A, Huang W R, Hong K H, Ravi K, Fallahi A, Moriena G, Miller R J D and Kätner F X 2015 *Nat. Commun.* **6** 8486
- [21] Zhang D et al 2018 *Nat. Photon.* **12** 336–42
- [22] Zhang D et al 2019 *Optica* **6** 872–7
- [23] Hebling J, Fülöp J A, Mechler M I, Pálfalvi L, Töke C and Almási G 2011 Optical manipulation of relativistic electron beams using THz pulses arXiv:1109.6852
- [24] Gorbunov L M and Kirsanov V I 1987 *Sov. Phys. JETP* **66** 290–4
- [25] Marquès J R et al 1998 *Phys. Plasmas* **5** 1162–77
- [26] Matlis N H et al 2006 *Nat. Phys.* **2** 749–53
- [27] Popov V S 2004 *Phys.–Usp.* **47** 855–85
- [28] Chen K R and Dawson J M 1992 *Phys. Rev. Lett.* **68** 29–32
- [29] Rueter D and Morgenstern T 2014 *Ultrasonics* **54** 2141–50
- [30] Banerjee S et al 2012 *Phys. Plasmas* **19** 056703
- [31] York A G, Layer B D, Palastro J P, Antonsen T M Jr. and Milchberg H M 2008 *J. Opt. Soc. Am. B* **25** B137–46
- [32] Pai C H, Huang S Y, Kuo C C, Lin M W, Wang J, Chen S Y, Lee C H and Lin J Y 2005 *Phys. Plasmas* **12** 070707
- [33] Shvets G, Kaganovich I and Startsev E 2002 *Phys. Rev. Lett.* **89** 139301
- [34] Tikhonchuk V T 2002 *Phys. Rev. Lett.* **89** 209301
- [35] Kalmykov S, Englesbe A, Elle J and Schmitt-Sody A 2020 *Plasma Phys. Control. Fusion* **62** 045008
- [36] Andreev N E, Gorbunov L M, Kirsanov V I, Nakajima K and Ogata A 1997 *Phys. Plasmas* **4** 1445–53
- [37] Sheng Z M, Meyer-ter-Vehn J and Pukhov A 1998 *Phys. Plasmas* **5** 3764–73
- [38] Andreev N E, Cros B, Gorbunov L M, Matthieussent G, Mora P and Ramazashvili R R 2002 *Phys. Plasmas* **9** 3999–4009
- [39] Landau L D, Lifshitz E M and Pitaevskii L P 2008 *Electrodynamics of Continuous Media* 2nd edn (Oxford: Butterworth-Heinemann)
- [40] Smith S J and Purcell E M 1953 *Phys. Rev.* **92** 1069
- [41] Sun G-Z, Ott E, Lee Y C and Guzdar P 1987 *Phys. Fluids* **30** 526–32
- [42] Bulanov S, Naumova N, Pegoraro F and Sakai J 1998 *Phys. Rev. E* **58** R5257–60
- [43] Brantov A V, Esirkepov T, Kando M, Kotaki H, Bychenkov V and Bulanov S V 2008 *Phys. Plasmas* **15** 073111
- [44] Polyanskiy M N, Babzien M and Pogorelsky I V 2015 *Optica* **2** 675–81
- [45] Woodbury D et al 2018 *Opt. Lett.* **43** 1131–4
- [46] Kalmykov S Y, Englesbe A, Elle J and Schmitt-Sody A 2020 *J. Phys.: Conf. Ser.* **1596** 012060
- [47] Shaloo R J, Arran C, Corner L, Holloway J, Jonnerby J, Walczak R, Milchberg H M and Hooker S M 2018 *Phys. Rev. E* **97** 053203
- [48] Zgadzaj R et al 2020 *Nat. Commun.* **11** 4753
- [49] Gorbunov L M, Mora P and Solodov A A 2003 *Phys. Plasmas* **10** 1124–34
- [50] Dawson J M 1959 *Phys. Rev.* **113** 383–7
- [51] Gorbunov L M, Mora P and Ramazashvili R R 2003 *Phys. Plasmas* **10** 4563–6
- [52] Jackson J D 1998 *Classical Electrodynamics* 3rd edn (New York: Wiley) ch 6.5
- [53] Jackson E A 1960 *Phys. Fluids* **3** 831–3
- [54] Everett M J, Lal A, Clayton C E, Mori W B, Joshi C and Johnston T W 1996 *Phys. Plasmas* **3** 2041–6
- [55] Gradshteyn I S and Ryzhik I M 2007 *Tables of Integrals, Series, and Products* 7th edn (San Diego, CA: Academic)
- [56] Pataki A and Greengard L 2011 *J. Comput. Phys.* **230** 7840–52
- [57] Carley M 2013 *IMA J. Numer. Anal.* **33** 1048–62
- [58] Mora P and Antonsen T M Jr. 1997 *Phys. Plasmas* **4** 217–29
- [59] Kondratenko A N 1979 *Penetration of Fields Into Plasma* (Moscow: Atomizdat) ch 1
- [60] Means R W, Muschietti L, Tran M Q and Vaclavik J 1981 *Phys. Fluids* **24** 2197–207
- [61] Hinkel-Lipsker D E, Fried B D and Morales G J 1992 *Phys. Fluids B* **4** 559–75
- [62] Hinkel-Lipsker D E, Fried B D and Morales G J 1993 *Phys. Fluids B* **5** 1746–53
- [63] Zhang S, Yu J, Shou Y, Gong Z, Li D, Geng Y, Wang W, Yan X and Lin C 2020 *Phys. Plasmas* **27** 023101
- [64] Ferri J, Davoine X, Kalmykov S Y and Lifshitz A 2016 *Phys. Rev. Accel. Beams* **19** 101301
- [65] Vargas M et al 2014 *Appl. Phys. Lett.* **104** 174103